



# Photocatalytic hydrogen production over flame spray pyrolysis-synthesised $\text{TiO}_2$ and $\text{Au}/\text{TiO}_2$

Gian Luca Chiarello, Elena Sellì\*, Lucio Forni

Dipartimento di Chimica Fisica ed Elettrochimica, CIMA/INA and ISTM-CNR, Università degli Studi di Milano, via Golgi 19, I-20133 Milano, Italy

## ARTICLE INFO

### Article history:

Received 1 March 2008

Received in revised form 3 April 2008

Accepted 5 April 2008

Available online 18 April 2008

### Keywords:

Photocatalytic water splitting

Methanol photoreforming

$\text{H}_2$  production

Flame spray pyrolysis

$\text{Au}/\text{TiO}_2$

## ABSTRACT

A set of titanium dioxide and gold-modified titanium dioxide samples were prepared by flame spray pyrolysis (FP) and characterized by BET, XRD, HRTEM and UV-vis reflectance analysis. Their photocatalytic activity in hydrogen production in water suspension, either from water photosplitting or from methanol photoreforming, was tested in an expressly set up, closed recirculation laboratory scale photoreactor and compared to those of commercial  $\text{TiO}_2$  samples, including Degussa P25, pure rutile and pure anatase. The rate of hydrogen evolution ( $r_{\text{H}_2}$ ) increased with increasing the anatase content, pure anatase being the most active photocatalyst. Surface area and crystallinity, both key properties of photocatalysts, can be tuned up by properly setting FP operation parameters, including the selection of the organic solvent/fuel. In particular, FP-made  $\text{TiO}_2$  prepared from a xylene solution showed more active than P25. Finally,  $r_{\text{H}_2}$  increased by one order of magnitude in water photosplitting and by ca. 30 times in methanol photoreforming upon 1% gold addition on  $\text{TiO}_2$ .

© 2008 Elsevier B.V. All rights reserved.

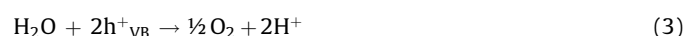
## 1. Introduction

The photocatalytic hydrogen production using solar energy is a challenging research topic which has received much attention in recent years for its potential to provide  $\text{H}_2$  as a clean and renewable energy resource even on a large scale [1]. This can be attained mainly by two processes, *i.e.* either by the direct splitting of water into hydrogen and oxygen [2], or by the photoreforming of organic compounds [2–5]. The latter process, occurring in the absence of oxygen, is very attractive especially when polluted wastewater is used as feed-stock, two goals being obtained in this case: the abatement of organic pollutants together with the production of hydrogen, an energy carrier.

In the last decade, different mixed metal oxides semiconductor photocatalysts, also with rather complex structure, such as layered or differently doped perovskite-based materials, have been proposed for water photosplitting [6–9]. However, titanium dioxide still remains the most suitable photocatalyst, in consideration of its high activity, chemical inertness, low cost and non toxicity [2,10].

Photocatalytic reactions on semiconductors are initiated by the absorption of a photon with energy equal to, or greater than, the

semiconductor bandgap. This promotes an electron from the valence band (VB) to the conduction band (CB), with the consequent formation of an electron ( $e^-_{\text{CB}}$ )-hole ( $h^+_{\text{VB}}$ ) pair. The so produced charge carriers can induce the reduction of electron acceptor species and the oxidation of electron donor species, respectively, both adsorbed on the semiconductor surface. In the case of water cleavage, the electron acceptor would be the  $\text{H}^+$  ion and the electron donor would be  $\text{H}_2\text{O}$ , according to the following reactions:



The overall photocatalytic water splitting formal reaction is, therefore:



Presently, one of the major problems in the exploitation of photocatalytic hydrogen production via water splitting over semiconductors is the low quantum efficiency of the process, consequent to the high probability of photogenerated electron-hole pairs recombination, releasing energy in the form of unproductive heat. Many efforts have been done in the last decades to increase the activity of semiconductor metal oxides,

\* Corresponding author. Tel.: +39 2 503 14237; fax: +39 2 503 14300.  
E-mail address: [elena.sellì@unimi.it](mailto:elena.sellì@unimi.it) (E. Sellì).

**Table 1**

Combustion enthalpy ( $\Delta H_c$ ) of the solvents employed in FP synthesis; specific surface area (SSA), from BET analysis, phase composition and crystallite dimensions, from XRD analysis, of the investigated  $\text{TiO}_2$  photocatalysts

Sample	Solvent/fuel	$\Delta H_c$ (kJ cm <sup>-3</sup> )	SSA (m <sup>2</sup> g <sup>-1</sup> )	Anatase		Rutile	
				wt%	$d_A$ (nm)	wt%	$d_R$ (nm)
FP1	Propionic acid	−20.6	66	56	27	44	37
FP2	2-Ethylhexanoic acid	−30.1	59	40	19	60	26
FP3	Propionic acid/methanol 2/8	−18.3	68	56	21	44	33
FP4	Xylene	−37.4	54	66	21	34	32
FP5	Xylene/pyridine 8/2	−36.7	106	90	11	10	8.6
Au/FP5	Xylene/pyridine 8/2	−36.7	106	90	10	10	9.0
P25	—	—	48	81	19	19	28
Anatase	—	—	285	100	5.6	0	—
Rutile	—	—	12	0	—	100	44

e.g. by adding “sacrificial agents” able to efficiently combine with  $e^-_{CB}$  or  $h^+_{VB}$ , or by modifying the photocatalysts by noble metal loading, to favour charge carriers separation.

Methanol and other organic species may act as sacrificial agents in photocatalysis, being able to combine with photogenerated valence band holes more efficiently than water (see reaction (3)). Thus, conduction band electrons become more readily available for reduction reactions, e.g. hydrogen production from water (reaction (2)). The presence of noble metal nanoparticles on the surface of semiconductor metal oxides can increase the electron–hole pair separation, because photopromoted electrons can be “captured” by the noble metal, if its Fermi level is lower in energy than the CB potential [2]. As electrons accumulate into the noble metal particle, their Fermi level shifts to more negative values, closer to the CB level of  $\text{TiO}_2$ , this upward shift being more negative, the smaller is the metal particles size [11]. Thus,  $\text{H}^+$  ions reduction to  $\text{H}_2$  over the noble metal surface is easier and more efficient than over  $\text{TiO}_2$ . Fig. 1 shows a schematic representation of the mechanism of photocatalytic water splitting over  $\text{Au}/\text{TiO}_2$ .

In the present work the photocatalytic activity in hydrogen production from water photosplitting of a series of  $\text{TiO}_2$  samples prepared by flame spray pyrolysis has been investigated, as well as the effect of both the addition of methanol and the deposition of gold nanoparticles on titanium dioxide.

Flame spray pyrolysis (FP) proved to be an effective method for the synthesis of nanosized  $\text{TiO}_2$  and noble metal-modified  $\text{TiO}_2$ , yielding high surface area, crystallinity, anatase content and better noble metal dispersion [12–15]. Furthermore, a FP-synthesised  $\text{TiO}_2$  photocatalyst was recently shown [15] to be more active than Degussa P25 in the photomineralisation of saccharides.

A FP apparatus for the preparation of different mixed oxides has been recently set up by our research group and the influence of the operation parameters on the properties of a series of

FP-synthesised perovskite catalysts have been investigated in detail [16–19]. In the present work the FP synthesis of  $\text{TiO}_2$  has been optimised, focusing in particular on the effects that the organic solvent nature and operation conditions may have on the physicochemical properties of the produced powders and on their photocatalytic activity in water splitting and methanol reforming.

## 2. Experimental

### 2.1. Photocatalysts preparation

The  $\text{TiO}_2$ -based photocatalysts FP1–FP5 (Table 1) were synthesised by the FP method, starting from a solution prepared by dissolving titanium(IV)-isopropoxide (Fluka, purum), 0.15 M, in different organic solvents and employing the home-made apparatus fully described in ref. [16]. The liquid solution was fed at 3.1  $\text{mL min}^{-1}$  in the flame reactor and dispersed by oxygen (6  $\text{L min}^{-1}$ ) at 1.5 bar constant pressure drop across the nozzle (internal diameter, 1.5 mm). Samples FP5 and  $\text{Au}/\text{TiO}_2$ , this latter containing 1% gold nanoparticles, were synthesised at the Institute of Chemical and Bioengineering of ETH, Zurich, employing the flame pyrolysis apparatus and operation conditions described in ref. [14]. In the case of  $\text{Au}/\text{TiO}_2$ , the desired amount of gold precursor (dimethyl-gold(III)-acetylacetone, >99%, Strem) was dissolved in pure xylene, together with the Ti-precursor. Another 1%  $\text{Au}/\text{TiO}_2$  sample (Au/P25) was prepared via deposition of tetrakis(hydroxymethyl) phosphonium chloride-stabilised gold nanoparticles on Degussa P25  $\text{TiO}_2$ , as detailed elsewhere [20].

Degussa P25, together with a pure anatase (Millennium Chemicals) and a pure rutile (Tioxide) sample, was also investigated, for comparison.

### 2.2. Characterization methods

XRD measurements were performed on a Philips PW3020 powder diffractometer, by using the  $\text{Cu K}\alpha$  radiation ( $\lambda = 1.54056 \text{ \AA}$ ). The diffractograms were compared with literature data [21] for phase recognition. Quantitative phase analysis was made by the Rietveld refinement method [22–24], using the “Quanto” software [25]. The average size of the crystallites was obtained by the Scherrer equation. The most intense reflection peak of each phase (at  $2\theta = 25.4^\circ$  for anatase and at  $2\theta = 27.5^\circ$  for rutile) was fitted with a Gaussian function to obtain the integral breadth of the reflection.

The BET surface area was measured by  $\text{N}_2$  adsorption/desorption at 77 K on a Micromeritics ASAP 2010 apparatus, after out-gassing in vacuo at 300 °C for at least 6 h. For high-resolution and scanning transmission electron microscopy (HRTEM), the material was dispersed in ethanol and deposited onto a perforated carbon foil, supported on a copper grid. The analysis was done on a

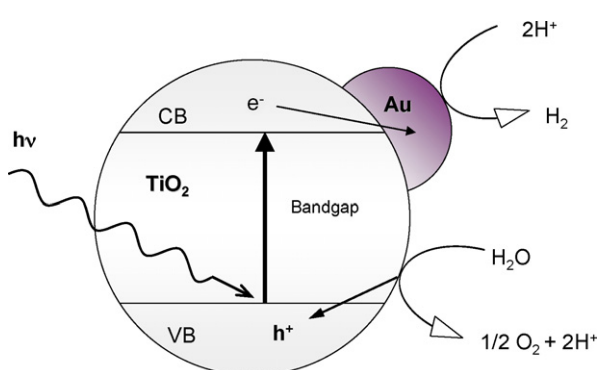


Fig. 1. Schematic representation of the mechanism of water photocleavage over  $\text{Au}/\text{TiO}_2$  semiconductor particles.

Tecnai F30 microscope (FEI, Eindhoven; field emission cathode) operated at 300 kV.

UV-vis diffuse reflectance was measured with a PerkinElmer Lambda 35 apparatus equipped with an integration sphere (Labsphere RSA-PE-20).

Thermogravimetric analysis (TGA) of the as prepared powders was carried out in flowing air by means of a PerkinElmer TGA7 apparatus, while heating the sample from 30 up to 800 °C at 10 °C min<sup>-1</sup>.

Temperature programmed oxidation (TPO) analysis was performed by means of the experimental apparatus described in detail elsewhere [26]. The photocatalyst (*ca.* 0.20 g) was loaded into a continuous, tubular quartz microreactor, fed with 30 cm<sup>3</sup> min<sup>-1</sup> of a 10% O<sub>2</sub> in He gas mixture and heated by an electric furnace, controlled by an Eurotherm 2408 TRC, with the same temperature ramp employed in TGA experiments. The composition of the out-coming gas was monitored by means of a quadrupolar mass spectrometer (QMS) (MKS, PPT Residual Gas Analyser).

### 2.3. Photocatalytic tests

The photocatalytic activity of the materials was tested in a closed recirculation laboratory scale photoreactor (Fig. 2), expressly set up to investigate the activity of suspended particles in water photosplitting, to produce H<sub>2</sub> and O<sub>2</sub>. The reactor consisted of a 45 mL, magnetically stirred cylindrical quartz vessel (A) containing the photoactive suspension, connected to a closed stainless steel circulation system, in which an inert gas (nitrogen) was continuously fluxed (100 mL min<sup>-1</sup>) by means of a bellow pump (C) (Metal Bellows, MB41E). The analysis of the species evolving from the aqueous suspension under irradiation and accumulating in the inert gas was done by a gas chromatograph (GC, Agilent 6890N) equipped with a molecular sieve column (MolSieve 5A) and with TC detector (D), using N<sub>2</sub> as carrier gas. The GC response was first calibrated by injecting known volumes of H<sub>2</sub> (or O<sub>2</sub>) into the recirculation system through a six ways sampling valve (E<sub>2</sub>).

The light source was an iron halogenide mercury arc lamp (Jelosil, 250 W), emitting in the 330–450 nm wavelength range (Fig. 2) with an irradiation intensity of  $1.67 \times 10^{-7}$  Einstein s<sup>-1</sup> cm<sup>-2</sup> on the

reactor, as determined by ferrioxalate actinometry [27]. All the photocatalysts (14 mg, corresponding to 0.3 g L<sup>-1</sup>) were suspended, either in pure water or in a 6 vol.% methanol aqueous solution, sonicated for 20 min and thoroughly flushed with inert gas in the photoreactor, before starting irradiation.

## 3. Results and discussion

### 3.1. Photocatalysts characterization

The different organic solvents or solvent mixtures employed as fuel in the synthesis of FP-photocatalysts are detailed in Table 1, together with the relevant properties of both FP and commercial photocatalysis. As evidenced in Fig. 3, the surface area of the FP-synthesised catalysts linearly decreases with increasing the combustion heat of the organic solvent/fuel employed. With increasing the combustion heat, the flame temperature becomes higher, with a consequent increase in the rate of particles growth. Thus, larger particles are obtained, possessing lower specific surface area. Similar results have been obtained in the FP preparation of perovskites [17–19].

According to XRD measurements (Fig. 4), all FP samples, similarly to P25, consist of a mixture of anatase and rutile crystal phases, in different percent amounts (Table 1). Brookite, the other TiO<sub>2</sub> polymorph, was never detected in our samples.

The quantitative phase analysis of the XRD patterns (Table 1) of samples FP1, FP2 and FP3, obtained from carboxylic acids solutions, revealed a higher rutile content with increasing the  $\Delta H_c$  of the Ti-precursor solvents, thus for higher flame temperature. However, the use of xylene, the solvent with the highest  $\Delta H_c$  value, led to a higher anatase content in sample FP4, which further increased up to 90% in the case of FP5. This points to a different TiO<sub>2</sub> formation mechanism in the flame when xylene, an apolar solvent, is used instead of carboxylic acids. Indeed, when the latter are mixed with Ti-isopropoxide the formation of titanium carboxylate and isopropanol can occur, a reaction which is not possible when the same titanium precursor is dissolved in xylene. Therefore, depending on the organic solvent/fuel, TiO<sub>2</sub> synthesis by FP can start from different titanium precursors, undergoing different oxidation mechanisms in the flame. Furthermore, as shown in Fig. 4, the XRD pattern of FP4 showed less diffuse scattering with respect to the other FP samples, indicating a higher crystallinity and a lower content of crystal defects. This may be ascribed to the

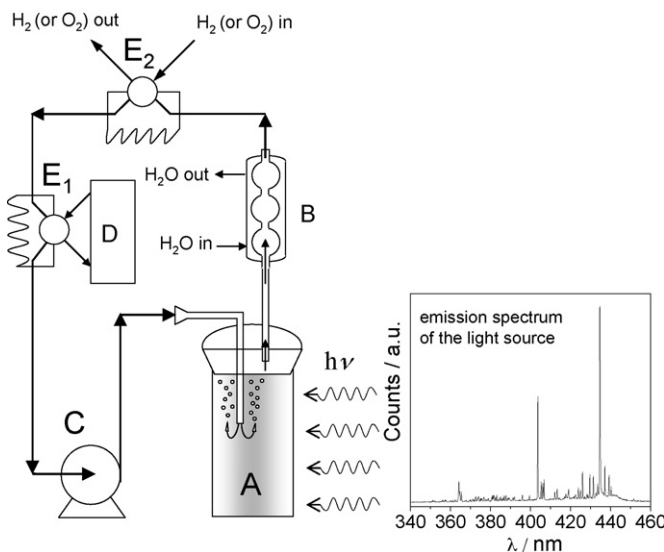


**Fig. 2.** Sketch of the experimental set up for photocatalytic activity measurements: (A) quartz reactor; (B) refrigerator-condenser; (C) bellow pump; (D) gas chromatograph GC with TC detector; (E<sub>i</sub>) six ways sampling valves.

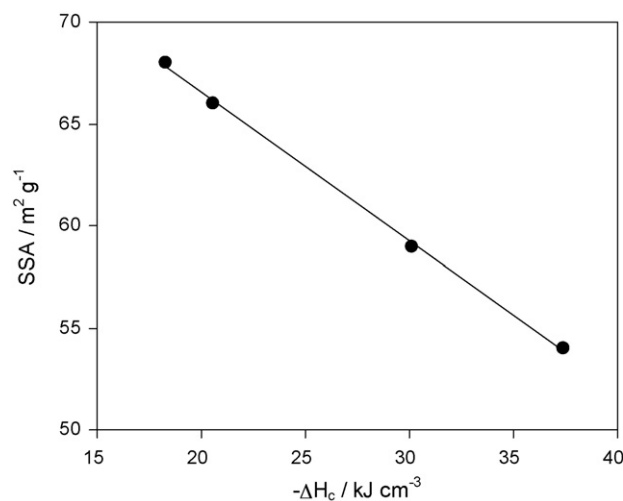


**Fig. 3.** Specific surface area SSA of FP samples vs combustion enthalpy of the solvents/fuels employed in FP synthesis.

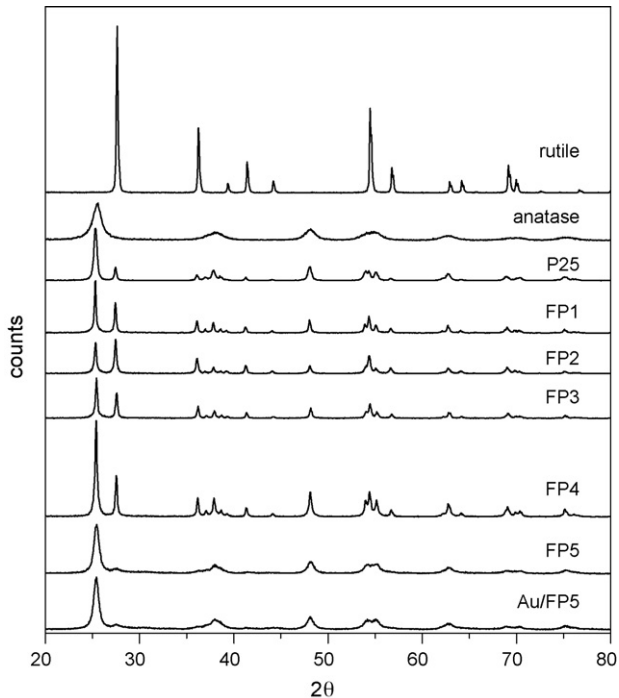


Fig. 4. XRD patterns of the investigated  $\text{TiO}_2$  samples.

much higher flame temperature produced by the xylene fuel [19]. Finally, it is worth noting that the presence of 1% gold in Au/FP5 did not affect the surface area and crystal structure (see Table 1 and Fig. 4). Similarly, such parameters did not vary after 1% Au nanoparticles deposition on  $\text{TiO}_2$  P25 in sample Au/P25.

Degussa P25, widely used as the benchmark photocatalyst for its outstanding photocatalytic activity in both oxidative and reductive paths, is synthesised through the Aerosil process, consisting in the hydrolysis of  $\text{TiCl}_4$  in a oxy-hydrogen flame. It has been shown to consist of separate anatase and rutile particles in contact, which provide favourable synergistic effects by leading to enhanced charge separation [28,29]. The FP samples show a very similar structure, with crystallite sizes even smaller than those of P25 (Table 1).

It is worth underlining that both the surface area and the anatase to rutile crystallite dimensions of FP materials depend on

the geometry of the burner employed for their synthesis. Indeed, sample FP5 possess a higher surface area ( $106 \text{ m}^2 \text{ g}^{-1}$ ) with respect to FP1–FP4 samples, most probably as a consequence of the more efficient dispersion of the liquid solution by the narrower nozzle. This would suppress the formation of the bigger particles, with the consequent increase of surface area. Furthermore, the FP1–FP4 samples exhibit smaller anatase crystallite size with respect to rutile crystallites, i.e.  $d_A/d_R < 1$ , as it is for P25, whereas  $d_A$  is larger than  $d_R$  for FP5 and Au/FP5, in agreement with very recent reports on a FP  $\text{TiO}_2$  sample presumably prepared with a similar burner [15]. As expected, the higher surface samples have smaller crystallite size (Table 1).

The HRTEM analysis showed highly crystalline and compact  $\text{TiO}_2$  particles, as witnessed by the clearly evident regular interference fringes (Figs. 5 and 6(b)). The presence of a bimodal distribution of the particle size, in which a majority of smaller particles ( $5 < d < 10 \text{ nm}$ ) is accompanied by some bigger particles ( $100 < d < 500 \text{ nm}$ ) can also be noticed in sample FP1 (Fig. 5). Au-loaded samples showed the presence of very small and well dispersed gold nanoparticles on the  $\text{TiO}_2$  surface, with a mean diameter around 1 nm (appearing as bright dots in Fig. 6(a)). Moreover, the average gold particle size (2 nm) of the FP-made Au/ $\text{TiO}_2$  was smaller than that of the gold-modified sample obtained by deposition of gold on Degussa P25 (Au/P25, see Fig. 6(b)). This confirms that FP is a very effective method to achieve excellent metal dispersion on high surface area  $\text{TiO}_2$ .

The as prepared FP materials can contain traces of carbonaceous residua, whose amount and nature depend mainly on the solvent nature [17–19]. Information on the nature and amount of such species can be obtained by TGA analysis coupled with TPO-QMS analysis. TGA curves recorded with different FP catalysts (Fig. 7) show that all samples lost surface adsorbed water in the 40–150 °C temperature range; the corresponding percent weight loss follows the order FP1 (0.8%) ≈ FP4 (0.8%) > FP3 (0.7%) > FP2 (0.5%). Higher temperature weight loss can be attributed [17–19] to the combustion (to  $\text{CO}_2$  and  $\text{H}_2\text{O}$ ) of organic compounds residua, in the 150–400 °C range, and to the decomposition of surface carbonates (to  $\text{CO}_2$  only), in the 400–600 °C range. According to TGA analysis, the amount of carbonaceous residua follows the order FP3 (2.5%) > FP1 (2.2%) > FP2 (1.4%) > FP4 (1%). Furthermore, the presence of surface carbonates is most evident in sample FP3, whereas FP4 contains the lowest, almost negligible amount of residua.

The bandgap values of our anatase and rutile  $\text{TiO}_2$  samples were calculated from the UV–vis absorption spectra reported in Fig. 8(a).

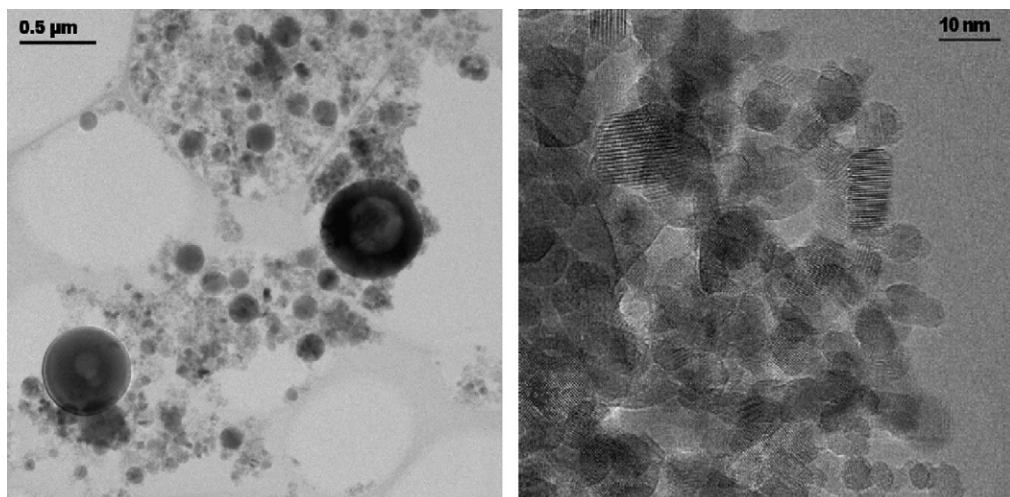
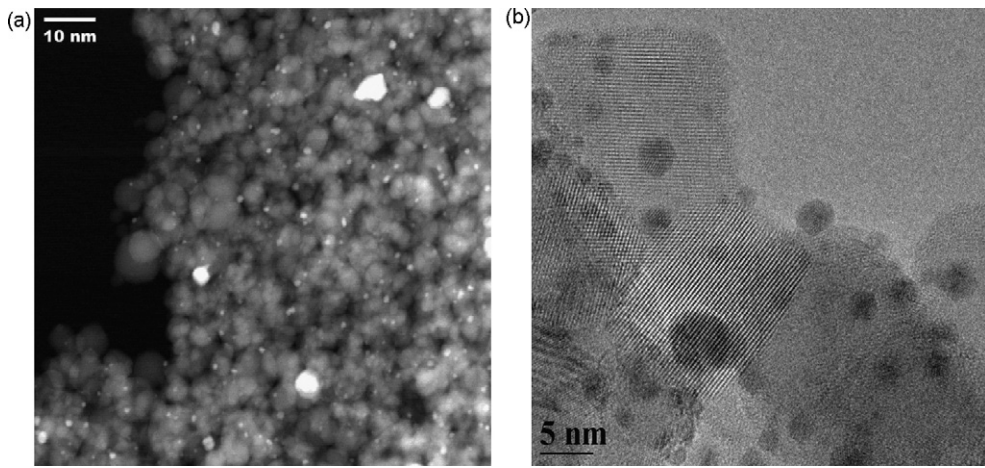


Fig. 5. HRTEM images of sample FP1.



**Fig. 6.** (a) TEM image of 1% Au/FP5: Au nanoparticles appear as bright dots; (b) HRTEM image of 1% Au/P25.

In particular, the threshold absorption wavelength ( $\lambda_0$ ) was determined from the second derivative of the absorption spectra, as the  $\lambda$  value at which a change in concavity occurs. The results show for anatase:  $\lambda_0 = 374$  nm and  $\Delta E_B = 3.2$  eV and for rutile:  $\lambda_0 = 407$  nm and  $\Delta E_B = 3.0$  eV, confirming that rutile has a slightly narrower bandgap with respect to anatase.

Detailed information on the shape of the absorption curves can be obtained from their first derivative plots shown in Fig. 8(b). Pure anatase and pure rutile give rise to a single peak first derivative, centred at 353 and 393 nm, respectively; P25 and FP1–FP5 samples, consisting of a mixture of anatase and rutile, exhibit more complex patterns. In particular, a sort of shoulder appears at relatively long wavelengths, perfectly matching the first derivative peak centred at 393 nm, and thus most likely attributable to rutile

absorption. On the other hand, in the 300–380 nm region the first derivative curves should be attributed to anatase absorption, although they appear to be split into two peaks, possibly indicating an interaction between rutile and anatase crystals in contact [28,29].

Finally, the gold-modified samples showed an additional absorption band in the visible region (Fig. 8(a)), which is responsible for their purple colour, *i.e.* the so called plasmonic absorption band. This absorption, typical of well separated gold nanoparticles in a colloidal suspension [30], is particularly evident in the absorption spectrum of Au/FP5, Au/P25 exhibiting a more flat absorption pattern extending in the visible region. The absorption maximum of Au/FP5 at 540 nm is red-shifted by  $18 \pm 2$  nm compared to the absorption peak at 522 nm of unsup-

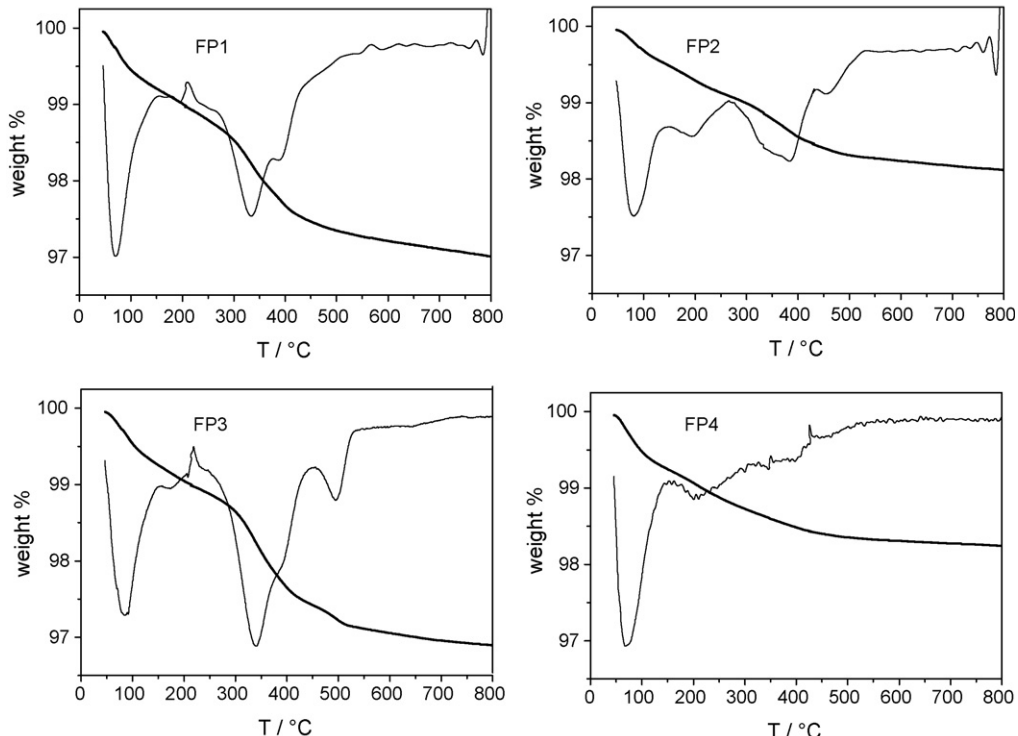


**Fig. 7.** Thermogravimetric analysis patterns (thick lines) and relative first derivative (thin lines) recorded during temperature programmed oxidation in 10%  $O_2/He$ . Heating rate  $10\text{ }^{\circ}\text{C min}^{-1}$ .

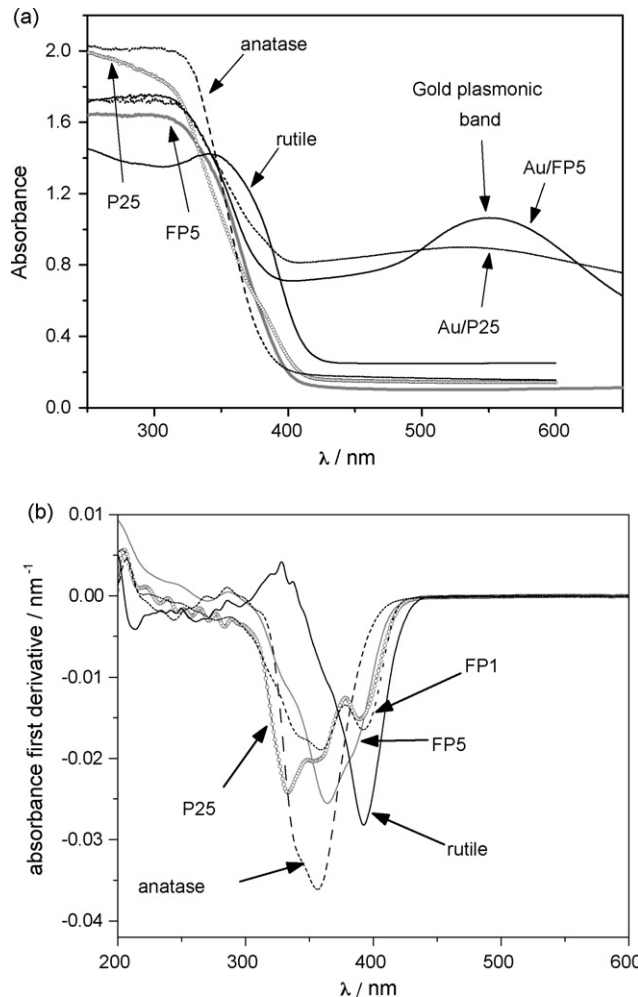


**Fig. 8.** (a) Absorption spectra and (b) their first derivative of the investigated  $\text{TiO}_2$ -based samples.

ported gold nanoparticles [30]. Such a red-shift was not observed for the FP-made  $\text{Au}/\text{SiO}_2$  and might indicate a weak interaction between gold and  $\text{TiO}_2$  [12].

### 3.2. Photocatalytic water splitting

The amount of  $\text{H}_2$  evolved under irradiation from aqueous suspensions containing different  $\text{TiO}_2$ -based photocatalysts is reported in Fig. 9. Hydrogen evolved at almost constant rate, except for a slight initial decrease in rate usually occurring within the first 2 h. The simultaneous  $\text{O}_2$  evolution was not monitored during the photocatalytic water splitting runs,  $\text{N}_2$  being employed as carrier gas in the optimised GC analysis of  $\text{H}_2$ .

Bare  $\text{TiO}_2$  photocatalysts exhibited low activity in water photosplitting. The values of constant hydrogen production rate ( $r_{\text{H}_2}$ , obtained as the slope of the linear part of the curves of Fig. 9) are collected in Table 2. FP-made  $\text{TiO}_2$  samples performed slightly better than commercial Degussa P25 ( $r_{\text{H}_2} = 3.04 \mu\text{mol H}_2 \text{ h}^{-1} \text{ g}_{\text{cat}}^{-1}$ ), FP4 and FP5 displaying similar  $r_{\text{H}_2}$  values, both ca. 1.6 times greater with respect to that of P25. This might be related to their higher surface area (see Table 1) and better crystallinity (Fig. 4).

Much better results were obtained over the gold-modified photocatalysts, confirming the beneficial effect of noble metal nanoparticles deposition. In particular, the FP-made sample proved to be the most active, with  $r_{\text{H}_2} = 52 \mu\text{mol H}_2 \text{ h}^{-1} \text{ g}_{\text{cat}}^{-1}$ . Its photocatalytic activity for hydrogen evolution is higher with

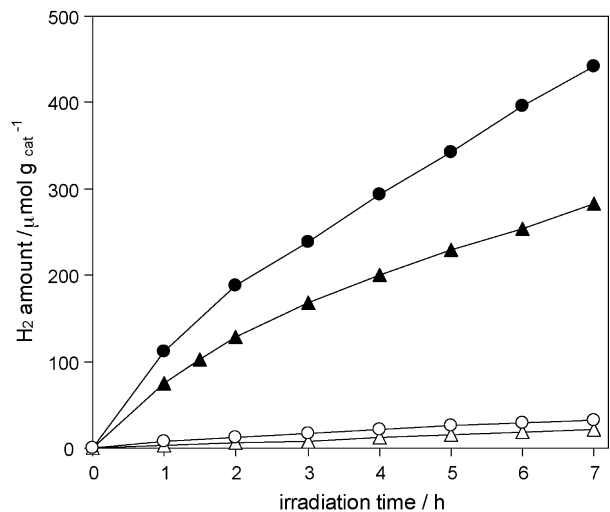


**Fig. 9.** Photocatalytic hydrogen production from pure water cleavage on (Δ) P25; (○) FP5; (▲) Au/P25; (●) Au/FP5.

respect to that of  $\text{Au}/\text{P25}$ , most probably because of its better gold dispersion, consequent to the smaller gold particles size (Fig. 6). Furthermore, by comparing the  $r_{\text{H}_2}$  values of the  $\text{Au}/\text{TiO}_2$  samples with those of the corresponding  $\text{TiO}_2$  samples, we find out that, in both cases,  $r_{\text{H}_2}$  increases by one order of magnitude upon 1% gold addition. Thus,  $r_{\text{H}_2}$  values seem to be tightly correlated also to the photocatalytic activity of the bare photocatalyst: the more active is this latter, the more active is the gold-modified photocatalyst.

Finally, for both gold containing photocatalysts the slight decrease of  $r_{\text{H}_2}$  within the first two irradiation hours (Fig. 9) might be ascribed to the presence of some carbon containing species on the photocatalysts (carbonaceous residua for  $\text{Au}/\text{FP5}$  or residual THPC stabiliser for  $\text{Au}/\text{P25}$ ). These species can act as more efficient hole scavengers with respect to water molecules, thus ensuring higher initial  $r_{\text{H}_2}$  values up to their complete oxidative photodegradation.

### 3.3. Photocatalytic methanol reforming

A significantly higher hydrogen evolution rate  $r_{\text{H}_2}$  was attained from water suspensions containing 6 vol.% methanol (see Figs. 10–12). Such methanol concentration (1.5 M) ensured maximum hydrogen production rate, no rate increase having been obtained for higher methanol amounts, whereas  $r_{\text{H}_2}$  was lower in more diluted methanol suspensions. It is worth underlining that only a very minor fraction (below 0.5%) of the initial methanol underwent photoreforming at the end of our runs. Methanol acts as an efficient hole scavenger, thus decreasing the  $e_{\text{CB}}-\text{h}_{\text{VB}}$  recombination rate and making conduction band electrons more readily available for  $\text{H}^+$  reduction.

The influence of stirring and bubbling of the recirculating gas was investigated first during methanol reforming on  $\text{TiO}_2$  P25. Indeed, the higher rate of hydrogen production attained in methanol reforming allowed a more easy control of the reaction

**Table 2**  
Hydrogen production rate ( $r_{\text{H}_2}$ ) in the photocatalytic splitting of pure water

Sample	$r_{\text{H}_2} (\mu\text{mol H}_2 \text{ h}^{-1} \text{ g}_{\text{cat}}^{-1})$	Relative rate
P25	3.04	1
FP5	4.90	1.6
Au/P25	30.3	10.0
Au/FP5	52.4	17.0

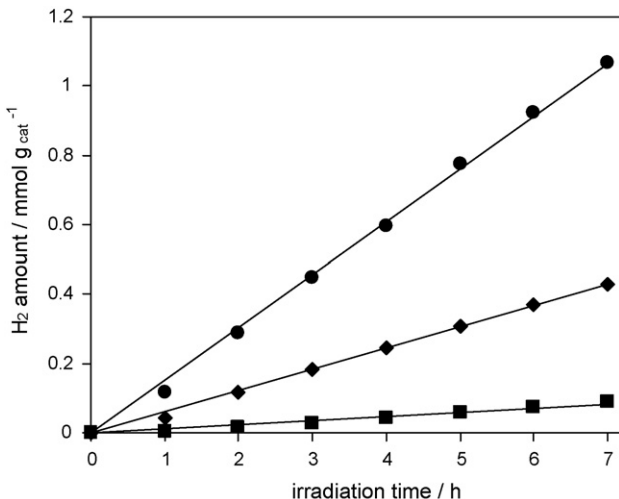


**Fig. 10.** Photocatalytic hydrogen production from methanol reforming under (■) no magnetic stirring and no gas phase bubbling; (◆) magnetic stirring and no gas phase bubbling; (●) magnetic stirring and gas phase bubbling.

conditions. The existence of mass transfer effects in the investigated system was thus established. In fact,  $r_{H_2}$  was higher under stirring than in the absence of stirring, as expected: stirring ensures a more efficient irradiation of the suspended photocatalyst particles, which would slowly deposit on the bottom of the reactor under standing conditions. Furthermore,  $r_{H_2}$  almost doubled when the recirculating gas was bubbled through the glass porous septum into the stirred suspension rather than simply flushed in the head space of the reactor, becoming 12 times greater with respect to that measured under standing conditions (see Fig. 10). Indeed, hydrogen photoproduced on the photocatalytic surface has to desorb and then diffuse through the liquid phase before reaching the gas phase. Therefore, all catalytic tests of both water splitting and methanol reforming were carried out under strictly controlled, constant rate magnetic stirring and gas phase bubbling into the irradiated suspension.

Fig. 11 reports the  $r_{H_2}$  profiles obtained in photoreforming of methanol over the different photocatalysts. Apart from pure rutile, all other samples showed a photocatalytic activity slightly increasing after the first irradiation hour. The origin of such initial induction effect most probably resides in the presence of the mentioned carbonaceous residua adsorbed on the  $TiO_2$  surface,

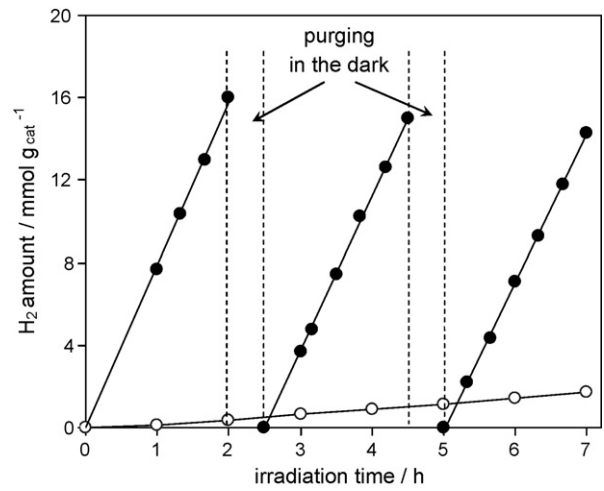


**Fig. 12.** Hydrogen production from photocatalytic methanol reforming on (○) FP5 and on (●) Au/FP5.

which are less effective electron donors than methanol. Only after their complete photocatalytic degradation all the adsorption surface sites become accessible to methanol. Indeed, this effect was minimal in the case of sample FP4, having the lowest carbonaceous residua content (Fig. 7). By contrast, with sample FP2, having the highest content of carbonaceous residua, the induction period exceeded 2 h, before reaching a linear trend.

The  $r_{H_2}$  values determined from the slope of the linear part of the Fig. 11 curves are listed in Table 3. They appear to increase with increasing the anatase content, according to the following activity scale (anatase percent content in brackets): pure anatase (100%) > FP5 (90%) > FP3 (56%) ≈ FP1 (56%) > FP2 (40%) > pure rutile. This is apparently in contrast with the  $H_2$  evolution rate results obtained with our recently developed photocatalytic water splitting device for separate hydrogen and oxygen evolution [31]. In that case we found that  $H_2$  evolved at a higher rate on a RF magnetron sputtering deposited  $TiO_2$  thin layer containing a higher amount of rutile. However, the higher wettability of anatase particles, ensuring an effective photocatalyst dispersion within the water suspension, together with surface area effects may play a more relevant role in the present study. In fact,  $r_{H_2}$  clearly increased with increasing the surface area of the  $TiO_2$  photocatalyst (Tables 1 and 3). Indeed, although P25 had a higher anatase content than FP2 (81% vs 56%, respectively), a slightly higher  $r_{H_2}$  was obtained with the FP-made photocatalyst (156 vs 177  $\mu\text{mol H}_2 \text{ h}^{-1} \text{ g}^{-1}$ , respectively), most probably because the lower anatase content was compensated by the higher surface area ( $48 \text{ m}^2 \text{ g}^{-1}$  vs  $68 \text{ m}^2 \text{ g}^{-1}$ , respectively). In addition,  $r_{H_2}$  increased with decreasing crystal defects. Indeed, crystal defects usually are detrimental in photocatalysis, because they can act as

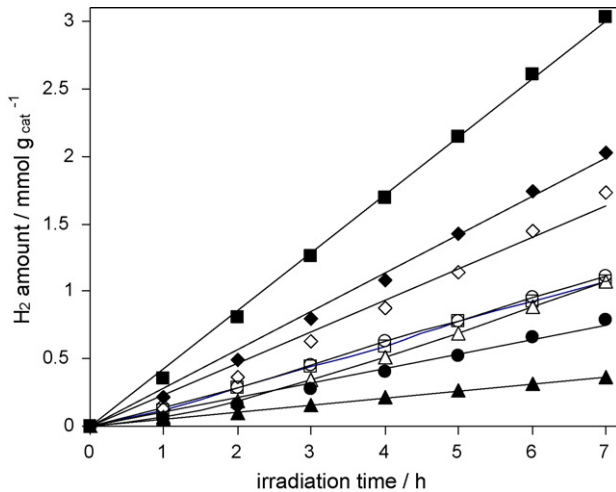


**Fig. 11.** Hydrogen production from photocatalytic reforming of methanol on (■) anatase; (◆) FP4; (◇) FP5; (○) FP1; (□) P25; (△) FP3; (●) FP2; (▲) rutile.

**Table 3**  
Hydrogen production rate ( $r_{H_2}$ ) from photocatalytic methanol reforming

Sample	$r_{H_2}$ ( $\mu\text{mol H}_2 \text{ h}^{-1} \text{ g}^{-1}$ )	Relative rate
Rutile	52	0.3
FP2	123	0.8
P25	156	1
FP1	158	1.0
FP3	177	1.1
FP5	266	1.7
FP4	297	1.9
Anatase	439	2.8
Au/FP5	7890	50

recombination centres for the photogenerated electron–hole pairs. FP4 proved to be the most active flame made sample, with a  $r_{H_2}$  similar to that of FP5, although the latter possessed higher surface area and higher anatase content. These two properties are compensated by the lower amount of crystal defects in FP4 (*vide supra*). Anyhow, apart from FP2, all of the other FP-made  $TiO_2$  photocatalysts displayed similar or even higher activity with respect to commercial Degussa P25.

Finally, a tremendous increase in  $r_{H_2}$  was attained with the FP-synthesised  $Au/TiO_2$  photocatalyst (Au/FP5, see Table 3). The activity was so high (6 NmL produced in 2 h), that purging with  $N_2$  was required every 2 h, to prevent  $H_2$  overpressure. Successive irradiation cycles were thus performed, with purging of  $N_2$  in the dark in between (Fig. 12). No induction period in hydrogen evolution on Au/FP5 was ever observed, with only a slight decrease in the  $H_2$  production rate in successive cycles (7890, 7530 and 7180  $\mu\text{mol H}_2 \text{ h}^{-1} \text{ g}_{\text{cat}}^{-1}$ , corresponding to *ca.* 215  $\text{NmL H}_2 \text{ h}^{-1} \text{ g}_{\text{cat}}^{-1}$ ). Thus,  $r_{H_2}$  determined with Au/FP5 was *ca.* 30 times higher than with the Au-free FP-photocatalyst (FP5). A beneficial role in photocatalytic methanol reforming of gold (and other metals) deposited on  $TiO_2$  P25 has been recently outlined by Bowker and co-workers [32,33]. The different experimental conditions adopted in such studies led to a lower hydrogen production rate on P25  $TiO_2$  and to a less than 15 times  $r_{H_2}$  increase upon gold deposition on this photocatalyst by the incipient wetness method. Furthermore, a mechanism fundamentally based on the adsorption of methanol oxidation intermediates on gold particles has been proposed. In our opinion, the high  $r_{H_2}$  values attained on  $Au/TiO_2$  are a direct consequence of the simultaneous beneficial effects of segregation of photopromoted electrons by gold nanoparticles and scavenging of photoproduced holes by methanol.

#### 4. Conclusions

Flame spray pyrolysis proved to be a very promising preparation method for the direct synthesis of  $TiO_2$ -based photocatalysts active in photocatalytic hydrogen production, by water splitting and especially by photoreforming of methanol. The proper selection of the FP-synthesis operation parameters allowed to tune up the physicochemical properties of the obtained powder. In particular, xylene proved to be the best solvent/fuel, leading to a FP- $TiO_2$  sample considerably more active than P25. The hydrogen production rate increased with increasing: (i) stirring and bubbling of the gas phase into the suspension, highlighting the presence of a mass transfer regime, at least in part; (ii) anatase content; (iii) surface area and (iv) crystallinity of the semiconductor photocatalyst, the latter being related to the decrease of crystal defects, brought about by the high temperature experienced by the forming particles during their travelling along the flame.

The highest rate of hydrogen production was attained with Au-modified titanium dioxide prepared by FP. Further addition of methanol to the irradiated reactant suspension led to an out-

standing increase in  $r_{H_2}$ , up to *ca.* 8 mmol of  $H_2/\text{h/g}$  of catalyst, *i.e.* 3 orders of magnitude greater than that obtained with the corresponding bare  $TiO_2$  and in the absence of methanol. In particular, the addition of gold entrained a 30-fold increase of  $r_{H_2}$  in methanol photoreforming, with respect to the rate obtained with the corresponding bare  $TiO_2$ .

#### Acknowledgements

We thank professor A. Baiker for providing the FP5 and Au/FP5 samples and professor L. Prati for providing the Au/P25 sample.

#### References

- [1] A.J. Bard, M.A. Fox, *Acc. Chem. Res.* 28 (1995) 141.
- [2] M. Ni, M.K.H. Leung, D.Y.C. Leung, K. Sumathy, *Renew. Sustain. Energy Rev.* 11 (2007) 401.
- [3] A. Patsoura, D.I. Kondarides, X.E. Verykios, *Appl. Catal. B: Environ.* 64 (2006) 171.
- [4] A. Patsoura, D.I. Kondarides, X.E. Verykios, *Catal. Today* 124 (2007) 94.
- [5] D.I. Kondarides, V.M. Daskalaki, A. Patsoura, X.E. Verykios, *Catal. Lett.* 122 (2008) 26.
- [6] Z. Zou, J. Ye, K. Sayama, H. Arawa, *J. Photochem. Photobiol. A: Chem.* 148 (2002) 65.
- [7] R. Abe, M. Higashi, K. Sayama, Y. Abe, H. Sugihara, *J. Phys. Chem. B* 109 (2005) 16052.
- [8] W. Yao, J. Ye, *Chem. Phys. Lett.* 435 (2007) 96.
- [9] H. Kato, A. Kudo, *Catal. Today* 78 (2003) 561.
- [10] A. Fujishima, T.N. Rao, D.A. Tryk, *J. Photochem. Photobiol. C* 1 (2000) 1.
- [11] V. Subramanian, E.E. Wolf, P. Kamat, *J. Am. Chem. Soc.* 126 (2004) 4943.
- [12] L. Mädler, W.J. Stark, S.E. Pratsinis, *J. Mater. Res.* 18 (2003) 115.
- [13] W.Y. Teoh, L. Mädler, D. Beydoun, S.E. Pratsinis, R. Amal, *Chem. Eng. Sci.* 60 (2005) 5852.
- [14] S. Hannemann, J.D. Grunwaldt, F. Krumeich, P. Kappen, A. Baiker, *Appl. Surf. Sci.* 252 (2006) 7862.
- [15] W.Y. Teoh, F. Denny, R. Amal, D. Friedmann, L. Mädler, S.E. Pratsinis, *Top. Catal.* 44 (2007) 489.
- [16] G.L. Chiarello, I. Rossetti, L. Forni, *J. Catal.* 236 (2005) 251.
- [17] G.L. Chiarello, I. Rossetti, P. Lopinto, G. Migliavacca, L. Forni, *Catal. Today* 117 (2006) 549.
- [18] G.L. Chiarello, I. Rossetti, L. Forni, P. Lopinto, G. Migliavacca, *Appl. Catal. B: Environ.* 72 (2007) 218.
- [19] G.L. Chiarello, I. Rossetti, L. Forni, P. Lopinto, G. Migliavacca, *Appl. Catal. B: Environ.* 72 (2007) 227.
- [20] M. Mrowetz, A. Villa, L. Prati, E. Sell, *Gold Bulletin* 40 (2007) 154.
- [21] M.D. Advanced Selected Powder Diffraction Data, J.C.P.D.S., Swarthmore, PA, 1974–1992.
- [22] D.L. Bish, S.A. Howard, *J. Appl. Cryst.* 21 (1988) 86.
- [23] R.J. Hill, C. Howard, *J. Appl. Cryst.* 20 (1987) 467.
- [24] H.M. Rietveld, *J. Appl. Cryst.* 2 (1969) 65.
- [25] A. Altomare, M.C. Burla, C. Giacovazzo, A. Guagliardi, A.G.G. Moliterni, G. Polidori, R. Rizzi, *J. Appl. Cryst.* 34 (2001) 392.
- [26] L. Forni, M. Toscano, P. Pollesel, *J. Catal.* 130 (1991) 392.
- [27] C.G. Hatchard, C.A. Parker, *Proc. Roy. Soc. (Lond.) A235* (1956) 518.
- [28] T. Ohno, K. Sarukawa, K. Tokieda, M. Matsumura, *J. Catal.* 203 (2001) 82.
- [29] D.C. Hurum, A.G. Agrios, K.A. Gray, T. Rajh, M.C. Thurnauer, *J. Phys. Chem. B* 107 (2003) 4545.
- [30] J. Turkevich, G. Garton, P.C. Stevenson, *J. Colloid Sci. Suppl.* 1 (1954) 26.
- [31] E. Sell, G.L. Chiarello, E. Quartarone, P. Mustarelli, I. Rossetti, L. Forni, *Chem. Commun.* (2007) 5022.
- [32] J. Greaves, L. Al-Mazroai, A. Nuhu, P. Davies, M. Bowker, *Gold Bulletin* 39 (2006) 216.
- [33] L.S. Al-Mazroai, M. Bowker, P. Davies, A. Dickinson, J. Greaves, D. James, L. Millard, *Catal. Today* 122 (2007) 46.